Available online at www.keaipublishing.com/en/journals/journal-of-magnesium-and-alloys/

ScienceDirect

Journal of Magnesium and Alloys 13 (2025) 5897–5910

www.elsevier.com/locate/jma

Full Length Article

Degradation and biocompatibility of Mg-Dy-Zn alloys containing the LPSO and γ' phases under physiological conditions

Genzhi Jiang[a], Yuanding Huang[a,*], Heike Helmholz[a], Nico Scharnagl[b], Ci Song[b], Zijian Yu[c,*], Yue Zhang[a,*], Regine Willumeit-Römer[a], Norbert Hort[a,d]

[a] *Institute of Metallic Biomaterials, Helmholtz-Zentrum Hereon, Max-Planck-Straße 1, Geesthacht, 21502, Germany*
[b] *Institute of Surface Science, Helmholtz-Zentrum Hereon, Max-Planck-Straße 1, Geesthacht, 21502, Germany*
[c] *College of Materials Science and Engineering, Beijing University of Technology, 100 Pingleyuan, Chaoyang District, Beijing, 100124, China*
[d] *Institute of Product Technology and Systems, Leuphana University Lüneburg, Universitätsallee 1, Lüneburg, 21335, Germany*

Received 17 March 2025; received in revised form 4 September 2025; accepted 15 September 2025
Available online 16 October 2025

Abstract

Previous work indicated that long-period stacking ordered (LPSO) phase and/or γ' in rare earth containing Mg biomaterials had contradictory mechanisms responsible for their degradation in less complex or standard salt media, such as 0.9 % NaCl solution. They needed to be further investigated in a more realistic simulated body fluid (SBF). The present work investigated the influence of the amount and types of intermetallics on the degradation behavior of as-cast Mg-xDy-Zn (x = 5, 10, 15 wt.%) alloys using immersion test in Dulbecco's modified Eagle's medium (DMEM) + Glutamax together with 10 % Fetal bovine serum (FBS) under cell culture conditions. It was revealed that the existence of intermetallics exhibited different effects on the degradation behavior of alloys. At the early stage of immersion, Mg-10Dy-1.5Zn alloy suffered the most serious degradation among these three alloys, owing to its more severe micro galvanic corrosion. With the immersion proceeding, the degradation rate of Mg-5Dy-1.5Zn alloy consistently increased because of the scattered distribution of few intermetallics. In contrast, the continuous network structure of intermetallics and a compact degradation layer provided protection from further degradation for Mg-10Dy-1.5Zn and Mg-15Dy-1.5Zn alloys. In the as-cast Mg-5Dy-1.5Zn alloy, only small amount of intermetallics composed of W, γ' and 18R LPSO phases acted as galvanic cathodes, accelerating its degradation. With Dy content increasing to 10 and 15 wt.%, large amounts of intermetallics including 18R LPSO and dense γ' phases were formed, which on the other hand can serve as a continuous network barrier to retard degradation propagation. Finally, the good adhesion and proliferation of the Human umbilical cord perivascular (HUCPV) on the surface of the Mg-10Dy-1.5Zn and Mg-15Dy-1.5Zn alloy indicated their good biocompatibility.

Keywords: Magnesium-dysprosium-zinc alloys; Network structure; Volume fraction; Degradation and biocompatibility; In vitro.

1. Introduction

Biodegradable implants have appeared as a valuable alternative in orthopedics over the past 2 decades and is projected to advance further in the coming years [1]. They reduce patients' pain, health risks and economic burden due to the avoidance of second surgery [2,3]. Magnesium (Mg) and its alloys which are biodegradable can be used as a temporary bone implant because of its good biocompatibility and closer density (1.74–2.0 g/cm^3), elastic modulus (41–45 GPa), tensile yield strength (120–180 MPa) and compressive yield strength (65–100 MPa) to those of natural bone [4]. Pure magnesium itself features unfavorable mechanical properties and corrosion resistance, which can affect implant stability and quickly change local chemical environment leading to cell death [5,6]. One way to promote its applications as implants is alloying with other elements to balance its degradation and mechanical properties [7–10]. Unfortunately, intermetallics can precipitate in most Mg alloys after alloying [11,12] and

---

Peer review under the responsibility of Chongqing University.

* Corresponding authors.

E-mail addresses: Yuanding.huang@hereon.de (Y. Huang), zijian.yu@bjut.edu.cn (Z. Yu), Yue.Zhang@hereon.de (Y. Zhang).

https://doi.org/10.1016/j.jma.2025.09.013

can greatly affect the subsequent micro galvanic corrosion. These intermetallics either act as a galvanic cathode to accelerate the degradation of matrix [13], or as a anode to dissolve priority [14]. The degradation of Mg alloys depends on the distribution, size and amount of these intermetallics [15].

Rare earth containing alloys such as Mg-Gd-Zn and Mg-Dy-Zn alloys show promising applications as implants owing to their high mechanical properties and biocompatibility [16,17]. The existence of long-period stacking ordered (LPSO) phase in their matrix can largely influence their corrosion resistance, especially their amount and distribution. For examples, in the Mg-Gd-Ni alloys [18], the 18R LPSO phase acts as a cathode. When its amount is low, the corrosion of Mg matrix is accelerated in 3 wt.% KCl solution. Conversely, a higher volume fraction 18R LPSO contributes to the formation of continuous corrosion barriers, which could reduce the degradation rate of Mg matrix [18]. Nevertheless, in the Mg-Zn-Y alloy, least volume fraction of 18R LPSO phase showed the best corrosion resistance in the 0.1 M NaCl solution [19].

Besides the 18R LPSO phase, the lamellar structure, generally accompanying with 18R LPSO phase [20,21], also play an important role in the corrosion of Mg alloys. Such lamellar structure can be the intermetallics, like γ' phase with a single unit cell height and an atomic stacking sequence of ABCA after melting or short-time low-temperature homogenization [13,22], or like lamellar 14H-LPSO phase has two ABCA-type building blocks after high temperature homogenization treatment [23]. In addition, the lamellar structure can be clarified as stacking faults (SFs). They are small ribbons, generally belonging to the intrinsic stacking faults I2 that is bounded by two Shockley partial dislocations [24]. The effects of lamellar structure on the corrosion behavior have been reported by different works. In the Mg-Er-Ni [13] and Mg-Gd-Ni [18] alloys, the existence of the higher proportion of lamellar 14H LPSO and/or γ' phases lead to the higher corrosion rate in the 3 wt.% KCl solution [13,18]. Thus, these lamellar second phase were regarded as cathode which could accelerate the corrosion behavior of Mg alloy [25–27]. In the Mg-Er-Zn [28] and Mg-Ho-Zn alloys [29], SFs were preferentially dissolved in the simulated body fluid (SBF) solution. They acted as the local anodes compared to the Mg matrix, thus protecting Mg matrix. Further, the SFs in the Mg-Er-Zn-Zr showed anode potential which was verified by experiments [20,30].

Although the influence of 18R LPSO and lamellar structure on the corrosion behavior of Mg alloys has been investigated, a complicated immersion environment could introduce their distinct corrosion behaviors [31,32]. Therefore, it’s necessary to explore the detailed effects of distribution, volume fraction and microstructure of 18R LPSO and/or lamellar structure on the degradation behavior of the biodegradable materials under cell culture condition. Our previous work showed that Dy element plays a crucial role in adjusting the intermetallics microstructure, thus influence the degradation behavior of Mg-Dy alloy largely [33–38]. To introduce the 18R LPSO phase and/or lamellar structure in Mg-Dy-based alloys, Zn element was added to the Mg-Dy system.

Previous investigations on the corrosion behavior of Mg-Dy-Zn alloy were limited. Bi et al. [39]. found that as-cast Mg-2Dy-0.5Zn (at.%) alloys with large amounts of 18R LPSO and Mg_2Dy phase was less resistant to corrosion in 3.5 wt.% NaCl solution, as compared to the alloys with lower volume fraction of fine and homogeneous distribution $Mg_{24}Dy_5$. In this alloy, the existence of 18R LPSO shows relative detrimental corrosion compared to that of 14H LPSO phase [40]. Unfortunately, these investigations only used the simple electrolyte NaCl. Moreover, the effects of intermetallic amount on the degradation of Mg-Dy-Zn alloy are also unclear. Therefore, the present work investigated the degradation of as-cast Mg-xDy-1.5Zn (x = 5, 10, 15 wt.%) alloys in a more realistic Dulbecco’s modified Eagle’s medium (DMEM) + Glutamax together with 10 % Fetal bovine serum (FBS) under cell culture conditions. The biocompatibility of Mg-10Dy-1.5Zn and Mg-15Dy-1.5Zn were also evaluated, to prove the potential medical application.

2. Experimental

2.1. Material preparation

Mg-xDy-1.5Zn (x = 5, 10, 15 wt.%) (designated as AC5, AC10 and AC15, respectively) were prepared using direct chill casting process in a permanent mould [41]. High-Purity Mg (99.94 wt.% Magnesium Electron, Manchester, UK) was molten in a mild steel crucible under a protective atmosphere (Ar + 2 % SF_6). Pure Zn, pure Dy were then added into the melt at 750 °C. The melt was stirred for 30 min at 200 rpm and then poured into a mold preheated to 680 °C covered with a mould release agent (boron nitride). The filled crucible was held at 680 °C for 15 min with steady stream of gas protection. Finally, the melt was solidified by lowering the crucible into cooling water at a rate of 10 mm/s. When the crucible was fully immersed, it was kept in the cooling water for 10 s and then removed it from water tank. The actual chemical compositions of alloys were measured by Inductively coupled plasma - Optical Emission Spectrometry (ICP-OES, Spectro Analytical Instruments GmbH, Kleve, Germany) and spark spectrometer (spark OES, Spectro Analytical Instruments GmbH, Kleve, Germany).

2.2. Microstructural characterizations

Specimens for microstructural observations were ground with silicon carbide emery paper up to 2500 grit, followed by polishing with 1 μm diamond suspension (Cloeren Technology GmbH, Niederkrüchten, Germany) and oxide polisher suspension (OPS, Industrieservice Siegmund Bigott, Kaarst, Germany). After chemically etched in a solution of 8 g picric acid, 5 mL acetic acid, 10 mL distilled water and 100 mL ethanol, their microstructures were characterized by optical microscope (LEICA DMLM, Leica Microsystems Wetzlar GmbH, Wetzlar, Germany). The average grain size was determined using the linear intercept methods with AnalySIS pro. The volume fraction of intermetallics was statistically determined from regions captured by backscattered electron (BSE) micrographs using ImageJ software. The structures of second phases were determined by X-ray diffraction (XRD) on a diffractometer (D8 Advance, Bruker, Karlsruhe, Germany) equipped with Cu Kα. The diffraction patterns were collected by step scanning from 10° to 80° angle with a step size of 0.02°/s. Transmission electron microscopy (TEM, Thermo Fisher Scientific GmbH, Waltham, USA) and aberration-corrected high-angle annular dark-field scanning transmission electron microscopy (HAADF-STEM) were performed using FEI Titan Themis operating at 300 kV. TEM foils were prepared by mechanical grinding to a thickness of approximately 60 μm and then ion-polished to perforation using a Gatan Precision Ion Polishing System (GATAN 695). Thermodynamic predictions were performed using Theromo-Calc software (Thermo-Calc Software AB, Stockholm, Sweden) with the database 2024a.

Degradation layer and their morphology were observed by scanning electron microscope (SEM, Tescan Vega3 SB, Brno, Czech Republic) equipped with an energy dispersive spectroscopy (EDS). The cross-sectional micrograph of lamellae structure for EDS analysis were prepared using focused ion beam (FIB, Tescan LYRA3) *in-situ* lift-out technique. To decrease the damage during ion beam thinning and polishing, a platinum protective layer was deposited on the surface of degradation product. Laser scanning confocal microscope (LSM 800, ZEISS, Oberkochen, Germany) with 20×objective was used in air to characterize the morphology and roughness of the degradation surface. These degraded surfaces were then analyzed by the surface imaging and analysis software ConfoMap® ST (Digital Surf, Besançon, France).

2.3. Localized volta potential difference distribution

Scanning kelvin probe force microscopy (SKPFM) was performed to measure differences in volta potential fluctuation of different microstructure area of each sample by an atomic force microscopy (NanoWizard 4, JPK Instruments AG, Germany). The used cantilever (Budgetsensors Multi75E-G) was coated with Cr/Pt for conductivity and possessed a resonance frequency of 75 kHz and a force constant of 3 N/m, respectively. Data analysis was adapted by JPK Data Processing software (JPK Instruments AG, Version 6.4.12). The specimens for SKPFM were prepared with the same method used for OM observations. Their measurements were conducted immediately so that their possible oxidation could be avoided.

2.4. Immersion test

Weight loss tests were performed in DMEM+Glutamax ((+) 4.5 g/L D-Glucose, (+) Pyruvate, Life Technologies, Darmstadt, Germany)) together with 10 % FBS (PAA Laboratories, Linz, Austria) and 1 % Penicillin Streptomycin (PenStrep) under cell culture conditions (37 °C, 20 % O_2, 5 % CO_2, 95 % relative humidity) in the incubator (Fig. 1(a)). According to the standard ISO 10993-12 (2008), the samples were immersed in the medium at a ratio of 10 mL/g (medium/sample). Disc samples with a diameter of 9 mm and a height of 1.5 mm were machined from the as-cast ingots. They were ultrasonically cleaned by n-hexane, acetone and 100 % ethanol, and then sterilized in 70 % ethanol and dried. Six samples were duplicated for each alloy. A minimum of four specimens was statistically used for degradation rate analysis. During immersion, the medium was renewed each 2–3 days. The medium was collected for measuring the pH value (measured using a SENTRON ARGUS X pH-meter, Fisher Scientific GMBH, Schwerte, Germany) and osmolality (measured using a Osmomat 030, Gonotec, Berlin, Germany). The medium without specimens served as a control. After immersion, the degradation products on the sample surface were removed by immersing in chromic acid (180 g/L chromium (VI) oxide in ultrapure water, VWR international, Darmstadt, Germany) for 10 min at room temperature. Then these samples were rinsed in ultrapure water and 100 % ethanol. After being dried, the weights of samples were determined. The average degradation rate (DR) and degradation depth (Δh) were calculated using the following Eqs. (1) and (2) [42]:

$$\mathrm{DR} = \frac{\mathrm{k} \times \Delta \mathrm{m}}{\mathrm{A} \cdot \mathrm{t} \cdot \rho} \tag{1}$$

$$\Delta \mathrm{h} = \frac{\Delta \mathrm{m}}{\mathrm{A} \cdot \rho} \tag{2}$$

Where k is a constant (8.76×10^4, ensuring DR is in mm/y), Δm is the observed mass loss (g), A is the surface area (cm^2), t is the immersion time (h), and ρ is the density of alloy (g/cm^3). The actual densities of as-cast alloys were measured according to Archimedes' principle using 100 % ethanol as a fluid and a balance for weighting [11].

2.5. Cell culture

The samples were pre-incubated in complete DMEM under cell culture condition for 24 h to obtain a relatively stable surface after the first burst of degradation with adsorbed serum proteins for improved cell adhesion (Fig. 1(b)). The glass substrate was used as a control group. Then, the human umbilical cord perivascular (HUCPV) cells (HUCPV cells are mesenchymal stem cells (MSC) with a high proliferation rate and strong potential for differentiation into an osteogenic phenotype [43,44]) were seeded with amount of 1×10^4 cells on the Mg alloys and glass surface (in beforehand agarose coated the bottom of wells, 12 well plate). After allowing the cells to adhere for 30 min at room temperature, 2 mL of fresh culture medium were added to each well, and sample plates were transferred to incubator (37 °C, 20 % O_2, 5 % CO_2, 95 % relative humidity). Medium was renewed at each 2–3 days. After incubation of 7 days, the cell viability was evaluated by live/dead staining (Live/Dead Viability/Cytotoxicity Kit, Life Technologies, Darmstadt, Germany). Before staining, removing the old medium and washing carriers with fresh cell specific media without FBS, then removing the wash medium. After staining for 20 min in medium containing 1.6 μM Calcein AM, 2 μM ethidium homidimer-1

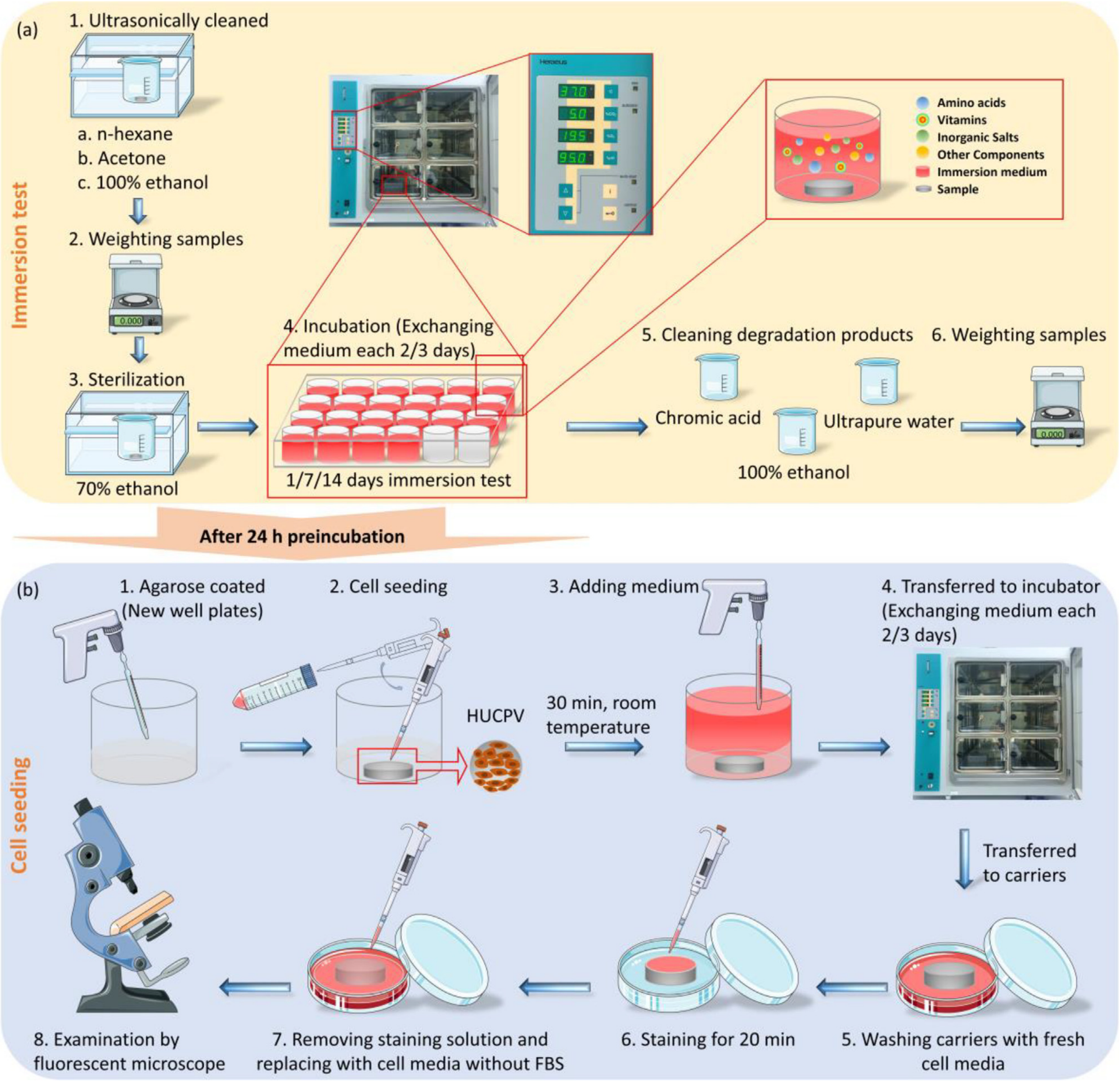

Fig. 1. Experimental flowchart of (a) immersion test and (b) cell seeding under cell culture conditions.

and 0.5 µg/mL Hoechst 33342, the staining solution was removed and replaced with cell media without FBS. Finally, the samples were examined with a fluorescent microscope (Eclipse Ni-E, Nikon, Düsseldorf, Germany) using a fluorescein isothiocyanate filter (excitation: 465–495 nm, emission: 515–555 nm) for living cells and a Texas Red filter (excitation: 540–580 nm, emission: 600–660 nm) for dead cells. The cell viability was quantitatively evaluated by counting nuclei using ImageJ software (v. 1.53e, NIH, USA).

2.6. Statistical analysis

All data were calculated as the average of at least three samples as technical replicates. The error bars were plotted based on the standard deviation. One-way analysis of variance (ANOVA) on ranks with Dunn's multiple comparison post hoc tests was adapted.

3. Results

3.1. Chemical composition

The actual chemical composition of as-cast Mg-Dy-Zn alloys are listed in Table 1. Due to the evaporation of raw material under the cast process, the actual chemical composition of Dy and Zn were lower than nominal composition. as listed in Table 1. The contents of impurities Fe, Ni and Cu are below the tolerance limits [45,46].

Table 1
Actual chemical compositions of alloys (wt.%).

Alloys	Dy	Zn	Fe	Cu	Ni	Ca	Mn	Al	Si	Be	Mg
AC5	4.51	1.39	0.0024	0.0008	0.0008	0.0026	0.0009	0.0063	0.0043	<0.0001	Balance
AC10	9.20	1.35	0.0031	0.0013	0.0008	0.0052	0.0009	0.0062	0.0098	0.0001	Balance
AC15	13.89	1.44	0.0043	0.0019	0.0007	0.0082	0.0010	0.0066	0.0145	0.0002	Balance

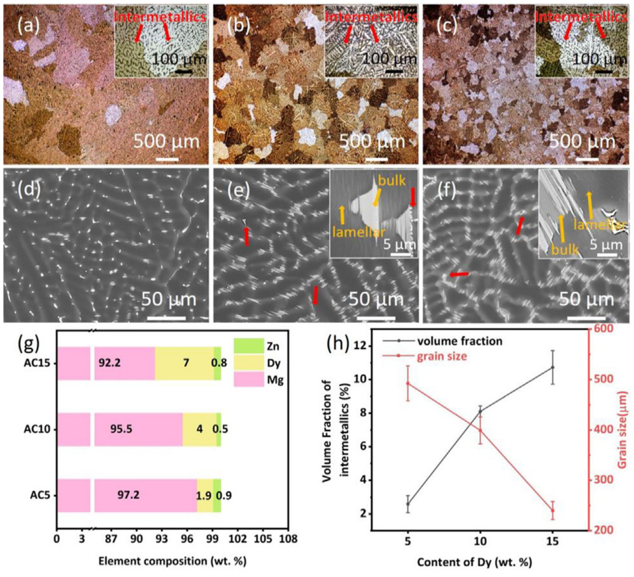

Fig. 2. OM and BSE microstructural images of (a and d) AC5, (b and e) AC10, (c and f) AC15 alloys, together with measured (g) composition of Mg matrix, (h) volume fraction of intermetallics and grain size.

3.2. Microstructural characterizations

The microstructures of as-cast Mg-Dy-Zn alloys with their volume fraction and grain size are shown in Fig. 2(a–g). The content of Dy increases in matrix when adding Dy from 5 wt.% to 15 wt.% (Fig. 2(g)), indicating that its solubility in matrix became higher and higher. The intermetallics were observed in the interdendritic space (Fig. 2(a–c)). BSE observations showed similar results to that depicted by OM (Fig. 2(d–f)). The lamellar structure was observed around the bulk phase in the AC10 and AC15 alloy (magnified BSE image in Fig. 2(e and f)). The morphologies obtained by BSE demonstrate that the amounts of intermetallics increases from 2.6 ± 0.5 % in the AC5 alloy to 10.7 ± 1 % in the AC15 alloy (Fig. 2(h)). Meanwhile, the grain size of as-cast Mg-Dy-Zn alloy significantly decreased. Among these three alloys, AC15 alloy has the smallest grain (Fig. 2(h)).

Fig. 3 shows TEM characterizations of second phase in these Mg-Dy-Zn alloys. The selected area electron diffraction (SAED) demonstrates the presence of α-Mg and W phase ($Mg_3Dy_2Zn_3$) with body-centered cubic (BCC) structures in AC5 alloy (Fig. 3(a)). Although W phase was not detected by TEM in the AC15 alloy, the combination of previously reported study [39] and the morphology observation from BSE imaging demonstrate that a negligible amount of W phases exist (marked by red arrows in Fig. 2(e and f)). In addition, a bulk second phase was observed in both AC5 and AC15 alloys. It was identified as 18R LPSO phase (Fig. 3(b–c, e, g)). Around the 18R LPSO phase and in the interdendritic space dense lamellar structure distributes. It was determined as γ' phase composing the single ABCA building block by HADDF-STEM [22,47,48] (Fig. 3(d and h)). Both the 18R LPSO phase and γ' exhibit the same crystal orientation inside the grain.

3.3. Degradation properties

3.3.1. Localized potential difference distribution of second phases

AC5 and AC15 alloys were selected for SKPFM measurements since in these two alloys 18R LPSO phase is the dominant. While in AC5 alloy both 18R LPSO and W phase are dominated. The AFM height mapping vaguely shows the signal for 18R LPSO phase in AC5 alloy (Fig. 4(a)). In contrast, the volta potential difference map clearly display the contrast difference between the second phase and matrix. Both 18R LPSO and W phases are brighter than Mg matrix (Fig. 4(b)). Further line-profile analysis (Fig. 4(c)) illustrates that the 18R LPSO phase showed a lower volta potential difference than the W phase. In the AC15 alloy the 18R LPSO phase has also a higher volta potential difference than the matrix (Fig. 4(e)). Its volta potential is higher in comparison with the matrix (Fig. 4(f)). Apparently, in these two alloys the second phases have a nobler volta potential than matrix. As indicated by Fig. 4(c and f), the volta potential difference of W phase with Mg matrix stands at approximately 250 mV for AC5 alloy, while the 18R LPSO phase at about 150 mV for AC5 alloy and 175 mV for AC15 alloy.

3.3.2. Degradation rates

Fig. 5(a) shows the degradation rate of as-cast Mg-Dy-Zn alloys under cell culture conditions. At the early stage of immersion (1 day), AC10 alloy exibits the most detrimental degradation. Although the amount of intermetallics in AC15 alloy is higher than that in other alloys, its degradation rate keeps low and even less than that of AC5 alloy where the amount of intermetallics is the lowest. At the later stage of immersion (7 and 14 days), the degradation rate of AC5 alloy consistently increases while the degradation rate of AC10 and AC15 alloys keeps realatively stable. It even reduces to the lower after long immersion for 14 days. After immersion for 14 days the degradation rate of AC15 alloy is only 0.10 mm/y. It is much lower than that of AC5 alloy with a value of 1.01 mm/y.

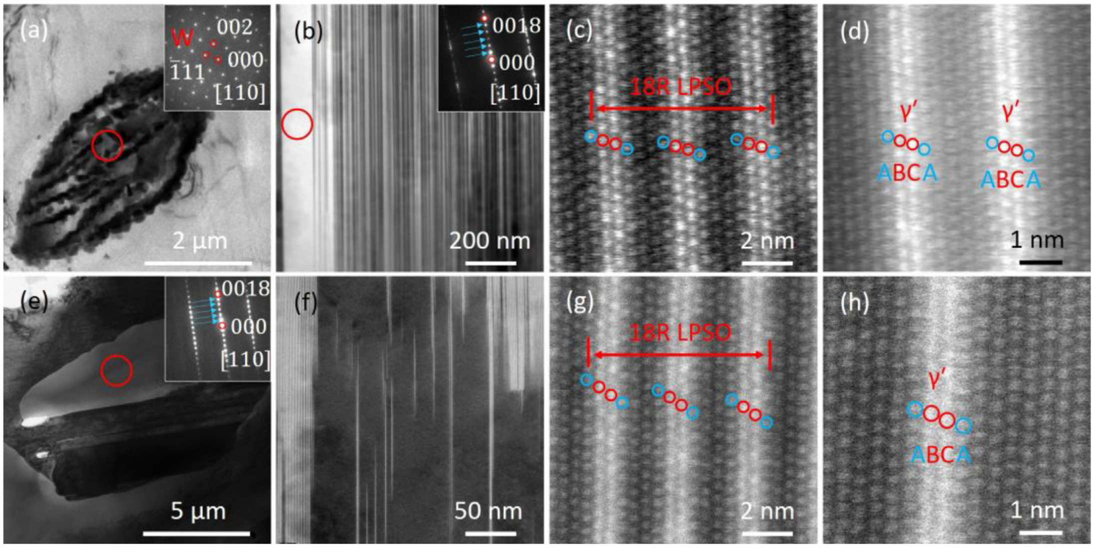

Fig. 3. TEM analysis of (a–d) AC5, (e–h) AC15. (a and e) Bright filed image, (b and f) HAADF images, (c–d, g–h) HAADF-stem images. The electron beam of HAADF-STEM is parellel to $[11\bar{2}0]_\alpha$.

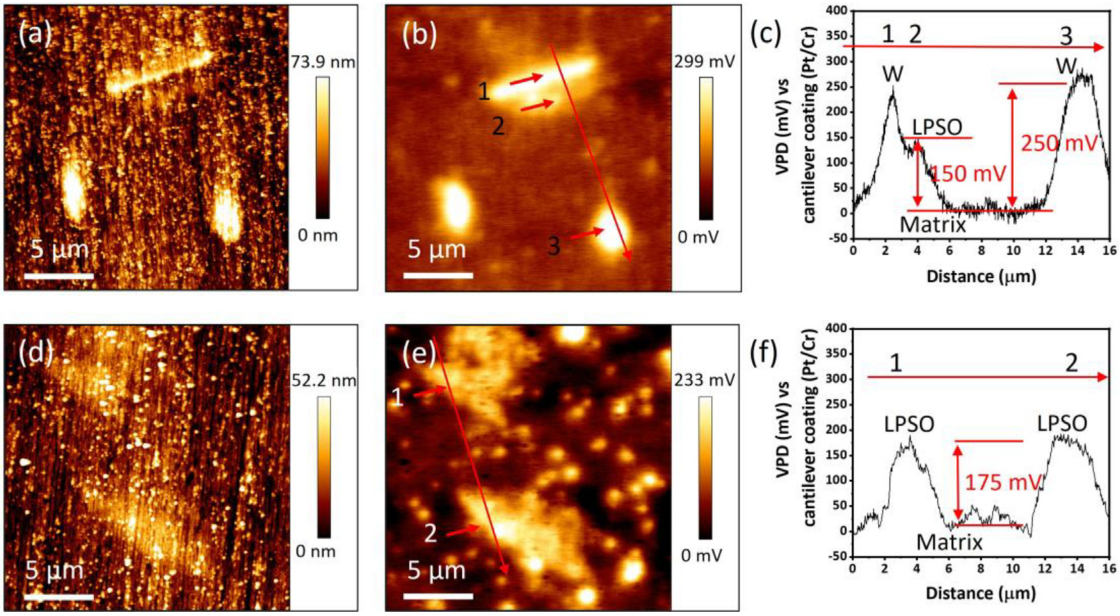

Fig. 4. SKPFM results of (a, b, c) AC5, (d, e, f) AC15 alloys. (a and d) Height map, (b and e) surface Volta potential difference (VPD) map, and (c and f) line-profile analysis of relative Volta potential difference distribution through intermetallic phases and Mg matrix, the numbers corerspond to intermetallics from (b) and (e).

The mean degradation depth was further calculated (Fig. 5(b)). It continuously increases with immersion continuing. At the early stage of immersion (1 day), the mean degradation depth of these three alloys have little difference. With the immersion proceeding (7 days), AC10 and AC15 alloys have close degradation depth, while AC5 alloy has a much higher degradation depth. When the immersion time reaches to 14 days, AC15 alloy still has a lower degradation depth than AC10 alloy. Its increment of degradation depth is small even after immersion for long time with 14 days. In contrast, the degradation depth of AC5 alloy increases largely. It exhibits a remarkable difference with other two alloys after long-term immersion.

The increase of pH and osmolality value was measured during each change of fresh medium (Fig. 5(c–d)). At the beginning of degradation, the increase of pH and osmolality is large for AC10 and AC15 alloy. The higher increase in pH value of AC10 at the 1 day of immersion indicates more OH^- release caused by extensive Mg matrix dissolution. With the immersion time increasing, they decrease till about 7 days. After immersion of 7 days, they rise stablely. Both the increments of pH and osmolality for AC5 alloy ex-

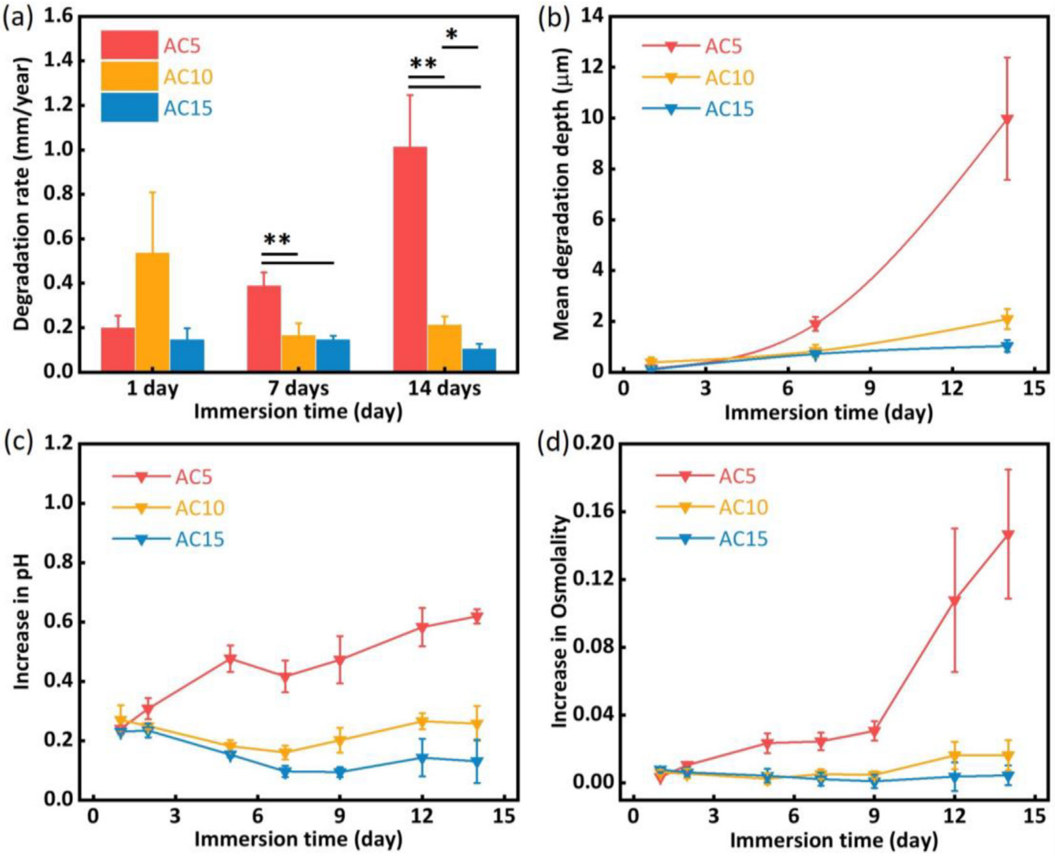

Fig. 5. Degradation properties for the as-cast Mg-Dy-Zn alloys, (a) degradation rate, (b) mean degradation depth, (c) increase in pH and (d) osmolality (the statistical significance level is: $** \ p < 0.01, * \ p < 0.05$, determined by one-way ANOVA, Dunn's test).

Table 2
Elemental compositions at the selected points in Fig. 6.

Analyzed position	Elements (at.%)					
	O	C	Dy	Ca	P	Mg
P1	59.31	11.52	0.41	1.02	1.71	Balance
P2	37.02	9.83	0.31	0.80	1.32	Balance

hibit a continuous increase with immersion proceeding. The overall changes of pH and osmolality are in agreement with that of degradation rate (Fig. 5(a)).

3.3.3. Morphological characterizations of degradation layer

BSE images of sample surfaces after immersion are shown in Fig. 6(a–l). The cracks were observed on the surface of samples. Their occurrence is due to the dehydrating when taking samples out from the immersion medium to air. For the AC5 alloy, the surface of degradation layer shows the different contrasts at the early stage of immersion (Fig. 6(a)). The darker region with wider degradation cracks (indicated as P1 in Fig. 6(a)) contains high contents of O, Ca, P and C (Table 2), demonstrating the formation of more calcium-phosphate and carbonate particles when compared with brighter area (indicated as P2 in Fig. 6(a)). As for AC10 and AC15 alloys, the network structure, which was formed by 18R LPSO and γ', was hardly corroded after immersion for 1 day. Even with the immersion proceeding to 14 days, no severe degradation was observed at the surface of interdenritic region (Fig. 6(e–f)). The distribution of network structure is uniform and its height consistent (Fig. 6(k and l)). In contrast, after immersion for 14 days the degradation surface of AC5 alloy exhibited different contrast. It is inhomogeneous with different heights due to the severe local corrosion around intermetallics.

The cross-sectional BSE observations with chemical element mapping were conducted from those samples immersed in DMEM + 10 % FBS medium for different time (Fig. 7). It can be seen that Dy exists in the degradation layer for all three alloys. This is in agreement with the EDS analysis shown in Fig. 8. After immersion from 1 day to 14 days Ca and P elements were enriched at the surface of degradation layer, indicating that the phosphate and calcium-phosphate were formed there. The formation of such a compact P/Ca-rich layer could inhibit the penetration of crossive ions in the DMEM+10 % FBS medium [49]. In addition, the determination of O, C, Ca, P and Mg elements revealed the formation of calcium-phosphate products and/or carbonate salts in the degradation layer [11]. Due to the existence of network structure in the AC10 and AC15 alloys non-continuous degradation layer can be found (Fig. 7(c–f)). In contrast, in the AC5 alloy severe

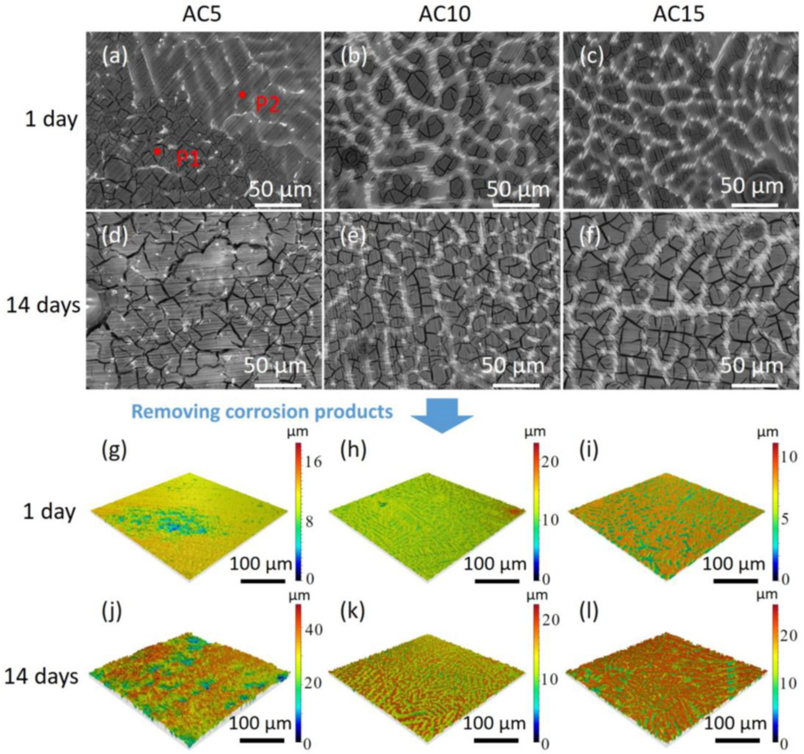

Fig. 6. (a–l) BSE images showing the surface morphologies of degradation layers of as-cast Mg-Dy-Zn alloys for different time. The topography of samples were obtained by laser confocal scanning after removing the degradation products, (g–i) 1 day and (j–l) 14 days.

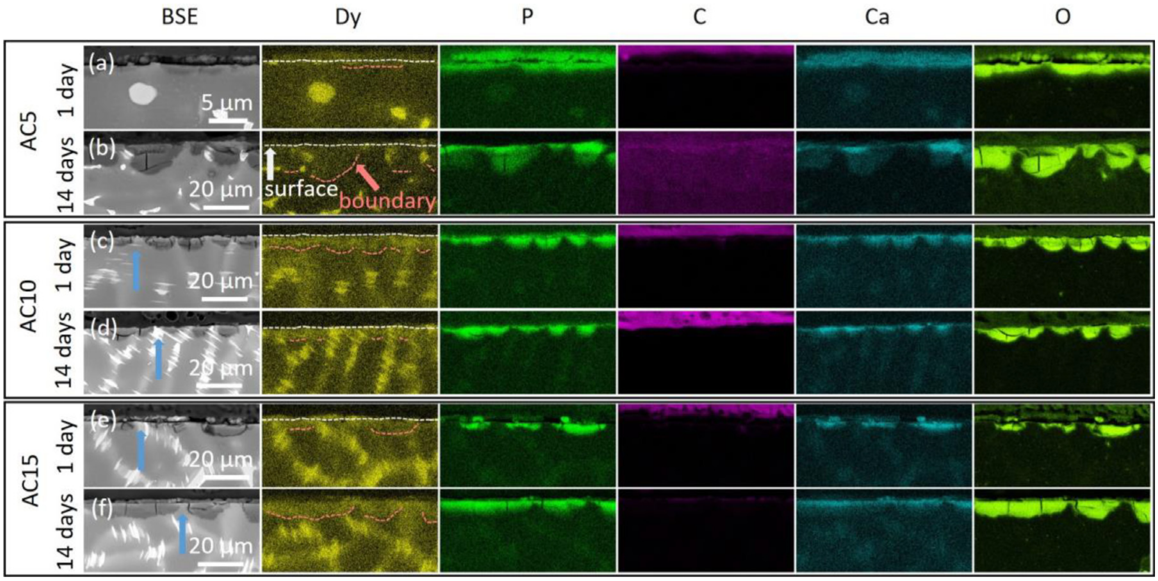

Fig. 7. Cross-sectional BSE micrographs and corresponding elemental mappings of (a and b) AC5, (c and d) AC10, (e and f) AC15 alloys exposed to DMEM+10% FBS under cell culture conditions for 1 day, 7 days and 14 days.

local corrosion happened leading to the embedding of the isolated intermetallics into the growth of degradation layer (Fig. 7(b)).

The degradation layer was further analyzed by EDS and XRD. The Ca content, Ca/P ratio and Dy content in the surface degradation layer after different immersion durations are shown in Fig. 8. At the earlier stage of immersion, the contents of Ca and Dy at the outer degradation layer of AC10 alloy are higher than that of other alloys. More Ca-Dy contained degradation products can be formed in the AC10 alloy at the early stage of its immersion suggest extensive matrix dissolution and accelerated reaction kinetics. With the degradation proceeding, the content of Ca in the outer degradation layer increases for all the alloys. Among them, AC15 alloy

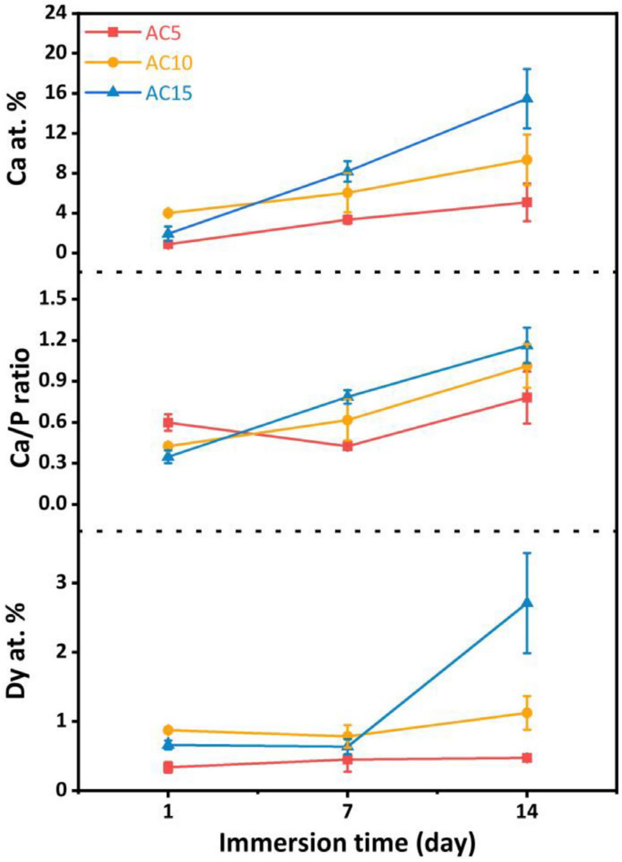

Fig. 8. Evolution of Ca content, Ca/P ratio and Dy content in the degradation layers with immersion time.

has the highest content of Ca in the surface of degradation layer, then followed by AC10 and AC5. All alloys maintain the stable Dy content in the outer degradation layer even when the immersion time is increased from1 day to 7 days. After 14 days of immersion, AC5 alloy still exhibits stable content of Dy in the degradation layer. However, in the degradation layers of AC10 and AC15 alloys, the content of Dy increased. Especially, it increases by 4 times, from 0.64 at.% to 2.71 at.%, for the AC15 alloy with the immersion time from 1 day to 14 days. Thus, more protective Ca-Dy contained compounds were formed in the degradation layer of AC15 alloy after it was immersed for 14 days. In addition, at the outer degradation layers of these two AC10 and AC15 alloys, the Ca/P ratio also monotonously increases with the immersion time. In contrast, Ca/P ratio in the degradation layer AC5 alloy shows a quite different evolution with immersion time. It has a "V" shape, i.e., first decreases and then increases.

Fig. 9 demonstrates the surface characterisations of as-cast Mg-Dy-Zn alloys after immersion for 1, 7 and 14 days by XRD. The characteristic peaks of as-cast alloys corresponding to W phase, 18R LPSO phase and α-Mg are agreement with that observed by TEM [50]. Due to the thin degradation layer, only few apparent characteristic peaks are observed for the degradation product of AC5 alloy. These peaks correspond to $CaCO_3$ (JCPDS No 41-1475).

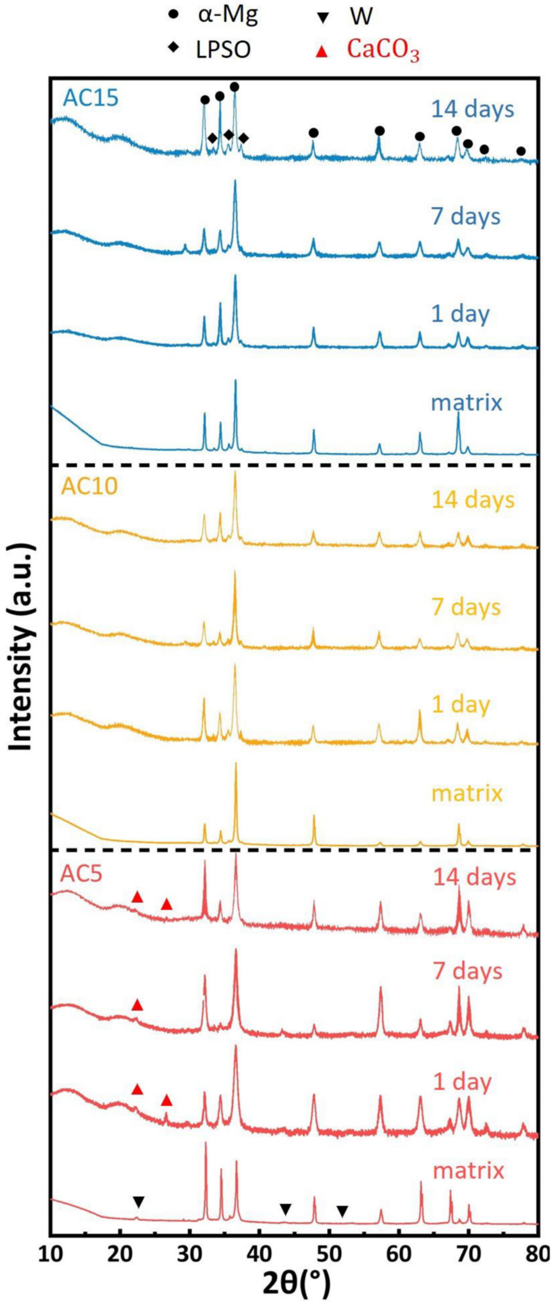

Fig. 9. XRD patterns of degradation layer after 1 day, 7 days and 14 days of immersion for the as-cast Mg-Dy-Zn alloys.

3.4. Cytocompatibility

The composition of degradation layer and environment of medium significantly influence cell adhesion and its viability [33]. The fast degradation rates can hinder the early cell adhesion on the sample surface. Consequently, the significantly increased degradation rate of the AC5 alloy, which results in a pH environment unfavorable for cell adhesion and survival (Fig. 5). Thus, it was excluded in cell experiments. Fig. 10 presents live/dead staining images of HUCPV cells after 168 h of incubation. Compared to the control group, most

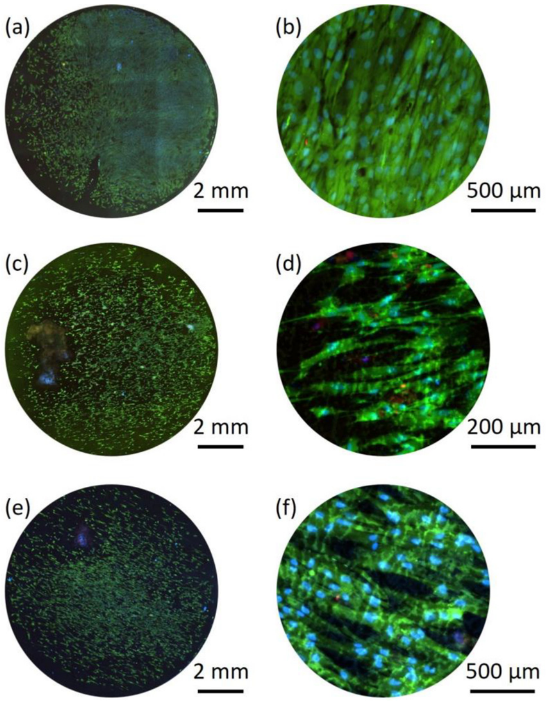

Fig. 10. Live/dead staining fluorescence images of HUCPV on the (a and b) glass substrate, (c and d) AC10 and (e and f) AC15 alloys samples after their incubation for 7 days.

of cells proliferate well and uniformly on the sample surface for AC10 and AC15 alloys. As shown in Table S1, both AC10 and AC15 alloys maintained cell viability above 70 % at 168 h, indicating their non-cytotoxic based on ISO 10993-5 standards [51]. While AC10 showed slightly lower cell viability than AC15, this may be attributed to minor experimental variations such as local pH fluctuation or inconsistencies in surface preparation, which can influence cell response in long-term cell seeding assays. Furthermore, Table S1 also provides a comparison with literature-reported viability values of other Mg alloys, including Mg-Zn [52], Mg-REs [33,53,54], Mg-Zn-Zr-Mn [51] systems, which typically show cell viability in the range of 70 %−90 %. The widely used WE43 alloy exhibits cell viability 75 %−95 % under similar conditions [55,56]. These comparisons demonstrate that the AC10 and AC15 alloys possess acceptable biocompatibility. Thus, the lack of severe cytotoxicity in alloys indicates that up to 15 wt.% Dy content, the Mg-Dy-Zn alloys remain acceptable for biocompatibility.

4. Disucussion

According to the phase diagram of Mg-xDy-1.5Zn alloys, the α-Mg phase crystallizes preferentially during the solidification process (Fig. S1). As the solidification temperature decreases, LPSO phases and γ' phases formed in the interdendritic space, followed by the low-melting-point W phase [57]. As a result, in the AC5 alloy, the coexistence of W, LPSO and γ' phases were observed (Fig. 3(a–d)). With the increase Dy content, the driving force for the nucleation and growth of the phases is enhanced, the segregation of Dy and Zn atoms was promoted, further promoting the formation of LPSO and γ' phases in the AC10 and AC15 alloys. Moreover, the preferential formation of LPSO and γ' phase consumed large amounts of Dy and Zn atoms, leading to the formation of abundant amounts of LPSO and γ' phases and only a minimal amount of W phase in the AC10 and AC15 alloys [57].

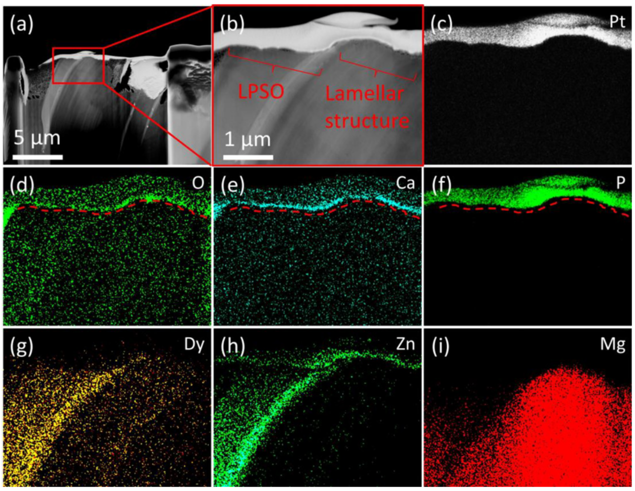

Fig. 11. (a) Dark field image, (b) local magnified image and (c–i) EDS mapping results of corroded surface for AC15 alloy exposed to DMEM+10 % FBS under cell culture conditions for 14 days.

As previously mentioned, the γ' phase commonly act as a cathodic that accelerates the degradation of the Mg matrix [13,18]. However, the γ' phase is observed to improve the corrosion resistance of Mg alloys in the present study. This apparent discrepancy could be attributed to differences in the degradation environments. It is well established that the stronger corrosive ability of the solution, such as sodium chloride, causes fast galvanic corrosion and simultaneously destroys the network structure formed by the 18R LPSO and dense γ' phases [58]. However, in the DMEM + 10 % FBS medium, galvanic corrosion leads to a local increase in pH due to Mg dissolution, which in turn promotes the precipitation of Ca^{2+} and PO_4^{3-} ions from the medium, forming Ca-P rich compounds [59–62]:

$$Mg + 2H_2O \rightarrow Mg^{2+} + 2OH^- + H_2 \uparrow \tag{3}$$

$$xMg^{2+} + yCa^{2+} + zPO_4^{3-} \rightarrow Mg_xCa_y(PO_4)_z \tag{4}$$

Importantly, the regular renewal of DMEM + 10 % FBS medium ensures a continuous supply of Ca^{2+} and PO_4^{3-}, thereby sustaining this protective deposition over time. Such Ca-P rich compounds layer exhibits superior corrosion resistance compared to conventional magnesium degradation products like $Mg(OH)_2$, thereby effectively protecting the underlying network structure [60,62]. As shown in Fig. 11, the EDS mapping reveals the element distribution of corroded surface for the AC15 alloy after 14 days of immersion. It can be observed that the lamellar structure area (γ' phase) is enriched

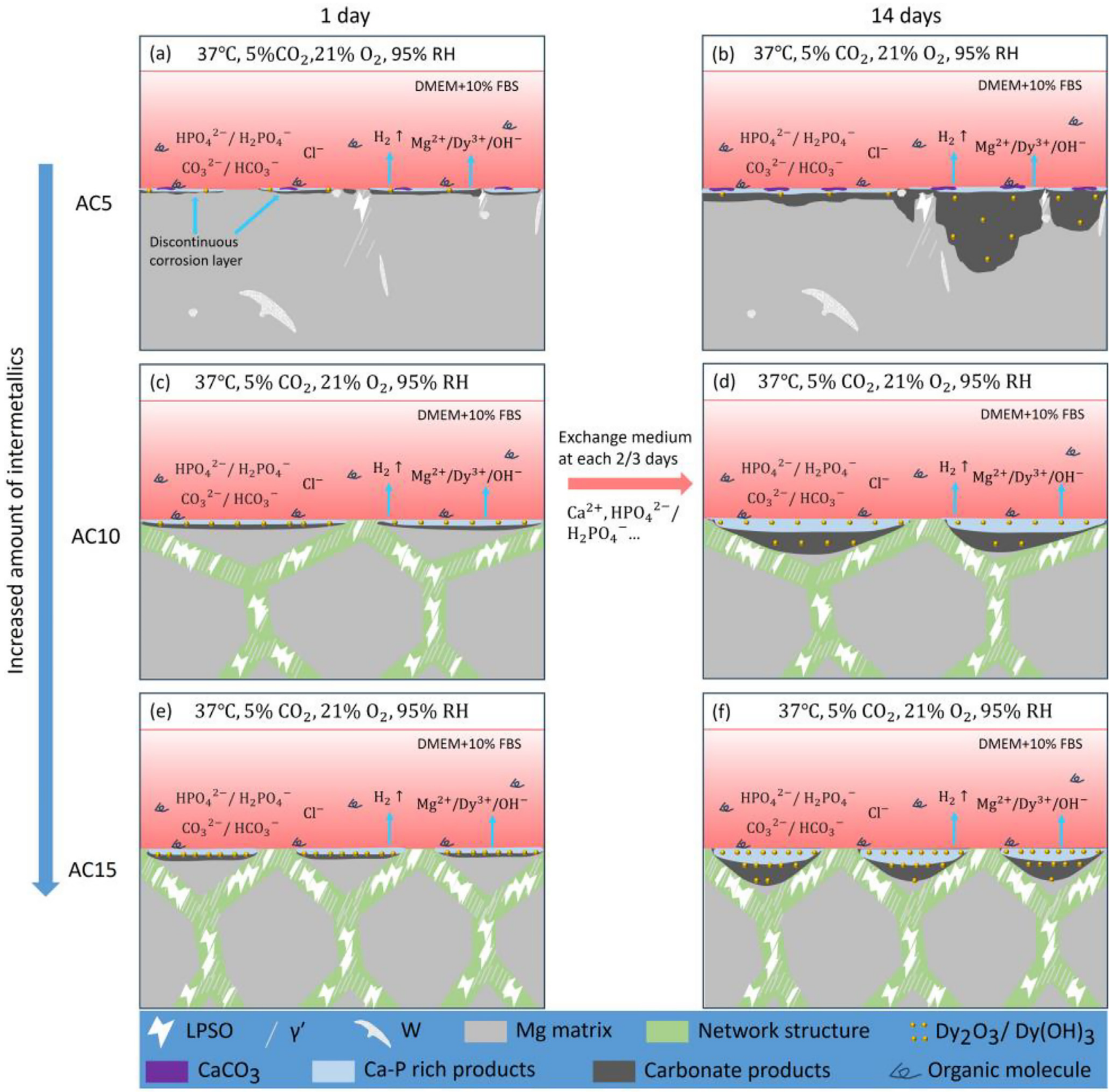

Fig. 12. Schematic illustrations of the (a and b) AC5, (c and d) AC10 and (c and d) AC15 alloys exposed to the medium for (a–c) 1 day and (b–d) 14 days. RH: Relative Humidity.

with Mg, along with lower concentrations of Dy and Zn compared with 18R LPSO phase. While significant enrichment of O, Ca, and P is evident on the surface of both 18R LPSO phase and lamellar structure. The Ca-P product layer plays a vital role in corrosion protection by serving as a physical barrier that limits the penetration of the solution along the compact γ' phase. This barrier effect reduces the exposure of the matrix to aggressive ions, thereby suppressing galvanic corrosion between the γ' phase and the surrounding matrix. Therefore, the preservation of the network structure by deposited surface products (Ca-P rich layer) plays a significant role in hindering further degradation for the AC10 and AC15 alloys.

In the degradation product layer, apart from the protective Ca-P layer, rare earth elements also contribute to the formation of the product layer. Such rare-earth-containing products can inhibit the attack of chloride ions on the Mg matrix [11,63,64]. Similar rare earth containing product layers are also observed in this study. The cross-sectional EDS mapping of degradation layer shows that the Dy compounds are enriched in the degradation layer (Fig. 7). Such rich Dy compounds are possible dysprosium oxide and/or dysprosium hydroxide [33,36,65], and could be possible formed by:

$$2\mathrm{Dy} + 3\mathrm{H_2O} \rightarrow \mathrm{Dy_2O_3} + 3\mathrm{H_2} \tag{5}$$

$$2\mathrm{Dy} + 6\mathrm{H_2O} \rightarrow 2\mathrm{Dy(OH)_3} + 3\mathrm{H_2} \tag{6}$$

Dy_2O_3 is insoluble in water. Due to the low solubility of $Dy(OH)_3$ (the solubility products constant (K_{sp}) of $Dy(OH)_3$ is 1.4×10^{-22} [64], which is smaller than $Mg(OH)_2$ (K_{sp}: 5.6×10^{-12}) .), the concentration of Dy^{3+} can reach saturation quickly, leading to the priority precipitation of Dy hydroxide than $Mg(OH)_2$ on the surface [63]. These two insoluble Dy-containing compounds can inhibit anions (Cl^-) from penetrating the substrate through the medium. Furthermore, the Pilling-Bedworth ratio for Dy_2O_3 is approximately 1.26 [66,67]. which could improve compactness and adhesion of degradation products and provide protection for the matrix from further degradation [11]. Therefore, the increase in Dy content not only promotes the formation of a network structure but also facilitates the generation of more dense degradation products, such as Dy_2O_3 and/or $Dy(OH)_3$. Such products further enhance the corrosion resistance of the AC15 alloy.

To clear illustrate the corrosion mechanism of three alloys, Fig. 12 presents the schematic illustration of the degradation process of three Mg-Dy-Zn alloys from 1 day to 14 days. The degradation behavior of Mg alloys was heavily influenced by the amount and distribution of intermetallics [11]. Large amounts of the W and 18R LPSO phases, which have obviously nobler potential than the Mg matrix (Fig. 4), could accelerate the Mg matrix degradation. Given this, the AC5 should degrade slowest and AC15 fastest according to the intermetallics amount (Fig. 2(h)). However, at the early stage of immersion, the AC15 alloys showed the lowest degradation rate. This could be attributed to the larger amounts of intermetallics leading into a lower area of galvanic corrosion of Mg matrix. In particular, the relatively continuous network formed by the 18R LPSO and γ' phases may help reduce the number of micro-galvanic corrosion sites per unit area and delay corrosion propagation. While for the AC5 alloy, the incomplete and discontinuous degradation layer (Fig. 6(a and g), Fig. 12(a)) indicate that the low content of galvanic corrosion, but the insufficient barrier effect results in continued matrix exposure to the corrosive medium. Interestingly, the AC10 alloy with middle amounts of intermetallics among these three alloys exhibits the most severe degradation rate. This is due to the excessive number of galvanic corrosion formed, combined with an less compact network structure. As a result, more micro-galvanic corrosion sites are generated compared to AC5, and the less compact intermetallic distribution leads to greater exposure of the corrodible Mg matrix surface than in AC15 (Fig. 12(c and e)). At the later stage of immersion, after the complete degradation of Mg matrix on the surface of the AC10 and AC15 alloys, the network structure (blue arrows in Fig. 7) effectively inhibits further penetration of medium, thus preventing the deeper Mg matrix from further dissolving (Fig. 12(d and f)). This supports the hypothesis that the morphology and connectivity of intermetallics become dominant factors in long-term corrosion resistance. As a result, the AC15 alloy, which contains a higher amounts of network structure, exhibits a lower degradation rate than the AC10 alloy after immersion of 14 days. Moreover, the quantity and distribution of the W phase in the AC10 and AC15 alloys (marked by red arrows in Fig. 2(e–f)) have a limited effect on the degradation rate, primarily due to its negligible amount. In the AC5 alloy, the scattered distribution of the intermetallics is insufficient to inhibit the penetration of degradation medium, leading to the deeper matrix corrosion (Fig. 12(b)). Meanwhile, the localized galvanic corrosion, induced by the intermetallics, results in an uneven distribution of the degradation product layer ((Fig. 6(j), Fig. 7(b)), and triggers the isolation of the intermetallics. This could emerge as another critical factor contributing to the monotonously increases of degradation rate. In comparison, for the AC10 and AC15 alloys, the continuous distribution network structure maintains their structural integrity, preventing isolation by degradation layer (Fig. 6(h–i, k–l)). Overall, the primary factors of intermetallics affecting degradation rates are their volume fraction at the early stage, while their morphology and distribution at the later stage. This dual-stage mechanism highlights the importance of both quantitative and distributed optimization of intermetallics for improved corrosion resistance.

5. Summary

The influence of intermetallics on the degradation behavior of as-cast Mg-Dy-Zn alloys with different contents of Dy were investigated by exposing to DMEM + 10% FBS medium for different durations. The influence of Dy content on biocompatibility of Mg-10Dy-1.5Zn and Mg-15Dy-1.5Zn alloys were evaluated. The main conclusions are listed as follows:

(1) The intermetallics in the as-cast Mg-xDy-1.5Zn (x = 5, 10 and 15 wt.%) alloys consist of W, 18R LPSO and γ' phase. The AC5 alloy possesses W, 18R LPSO and γ' phases, while the AC10 and AC15 alloy mainly contain the 18R LPSO and dense γ' phases. With the increment of Dy content, the volume fraction of intermetallics increases.

(2) At the early stage of immersion, the amounts of intermetallics act as the main role in affecting the degradation rate. Among these three alloys, the AC10 alloy with middle amounts of intermetallics showed the largest degradation rate at day 1. This could be due to more galvanic corrosion than AC5 alloy and less compact network structure (18R LPSO + γ' phases) compared with AC15 alloy.

(3) At the later stage of immersion, the morphology and distribution of intermetallics act as the main role in affecting the degradation rate. The AC15 alloy with largest amount of intermetallics showed the lowest degradation rate. This attributes to the network structure in it which suppresses further degradation propagation.

In contrast, in the AC5 alloy the effect of its scattered distribution of intermetallics on galvanic corrosion act as dominant role to continously increases its degradation rate.

(4) In AC10 and AC15 alloys, the formation of a rich Ca-P degradation layer on their surface of network structure prevents the dense γ' phases from causing severe galvanic corrosion with Mg matrix, thus preserving the integrity of the network structure.

(5) Mg-Dy-Zn alloy retains a good biocompatibility with the Dy content up to 15 wt.%.

Declaration of competing interest

Yuanding Huang is an editorial board member/editor-in-chief for Journal of Magnesium and Alloys and was not involved in the editorial review or the decision to publish this article. All authors declare that there are no competing interests.

CRediT authorship contribution statement

Genzhi Jiang: Writing – original draft, Methodology, Investigation, Formal analysis, Data curation, Conceptualization. **Yuanding Huang:** Writing – review & editing, Supervision, Methodology, Conceptualization. **Heike Helmholz:** Writing – review & editing, Investigation. **Nico Scharnagl:** Writing – review & editing, Investigation. **Ci Song:** Writing – review & editing, Investigation. **Zijian Yu:** Writing – review & editing, Investigation, Data curation. **Yue Zhang:** Writing – review & editing, Visualization, Formal analysis, Data curation. **Regine Willumeit-Römer:** Resources, Methodology. **Norbert Hort:** Writing – review & editing, Supervision, Resources, Methodology, Conceptualization.

Acknowledgments

Mr. Genzhi Jiang and Dr. Yue Zhang would like to thank the China Scholarship Council for the award of fellowship and funding (nos. 202106890013 and 202206095009). Dr. Yue Zhang also would like to thank German Academic Exchange Service (DAAD) for the award of fellowship and funding (no. 91870848). Mr. Gert Wiese, Ms. Anke Borkam-Schuster and Ms. Monika Luczak are gratefully acknowledged for their technical supports. HUCPV cells were provides by the Bethesda Hospital Hamburg - Bergedorf (Ethical approval PV5991).

Supplementary materials

Supplementary material associated with this article can be found, in the online version, at doi:10.1016/j.jma.2025.09.013.

References

[1] A.R. Khan, N.S. Grewal, C. Zhou, K. Yuan, H.-J. Zhang, Z. Jun, Results Eng. 20 (2023) 101526, doi:10.1016/j.rineng.2023.101526.

[2] Y. Liu, Y. Zheng, X.H. Chen, J.A. Yang, H. Pan, D. Chen, L. Wang, J. Zhang, D. Zhu, S. Wu, Adv. Funct. Mater. 29 (2019) 1805402, doi:10.1002/adfm.201805402.

[3] Y.F. Zheng, X.N. Gu, F. Witte, Mater. Sci. Eng. R. Rep. 77 (2014) 1–34, doi:10.1016/j.mser.2014.01.001.

[4] M.P. Staiger, A.M. Pietak, J. Huadmai, G. Dias, Biomaterials 27 (2006) 1728–1734, doi:10.1016/j.biomaterials.2005.10.003.

[5] S. Virtanen, Mater. Sci. Eng. B 176 (2011) 1600–1608, doi:10.1016/j.mseb.2011.05.028.

[6] C. Kammer, D. Aluminium-Zentrale, Magnesium Taschenbuch, Aluminium-Verlag, Düsseldorf, 2000.

[7] N. Hort, Y. Huang, D. Fechner, M. Stormer, C. Blawert, F. Witte, C. Vogt, H. Drucker, R. Willumeit-Römer, K.U. Kainer, F. Feyerabend, Acta Biomater. 6 (2010) 1714–1725, doi:10.1016/j.actbio.2009.09.010.

[8] D. Krüger, B. Zeller-Plumhoff, B. Wiese, S. Yi, M. Zuber, D.C.F. Wieland, J. Moosmann, R. Willumeit-Römer, J. Magnes. Alloys 9 (2021) 2207–2222, doi:10.1016/j.jma.2021.07.029.

[9] S. Zhou, A. Tang, T. Liu, Y. Huang, P. Peng, J. Zhang, N. Hort, R. Willumeit-Römer, F. Pan, J. Alloys. Compd. 947 (2023) 169669, doi:10.1016/j.jallcom.2023.169669.

[10] H. Wang, R. Cheng, B. Jiang, M. Yang, D. Deng, Z. Dong, J. Song, C. Yu, L. Chai, F. Pan, J. Magnes. Alloys 13 (2025) 894–901, doi:10.1016/j.jma.2024.01.010.

[11] Y. Zhang, Y. Huang, F. Feyerabend, C. Blawert, W. Gan, E. Maawad, S. You, S. Gavras, N. Scharnagl, J. Bode, C. Vogt, D. Zander, R. Willumeit-Römer, K.U. Kainer, N. Hort, Acta Biomater. 121 (2021) 695–712, doi:10.1016/j.actbio.2020.11.050.

[12] J. Gröbner, A. Kozlov, X.-Y. Fang, S. Zhu, J.-F. Nie, M.A. Gibson, R. Schmid-Fetzer, Acta Mater. 90 (2015) 400–416, doi:10.1016/j.actamat.2015.02.044.

[13] C. Dai, J. Wang, Y. Pan, K. Ma, Y. Peng, Y. Wang, D. Wang, C. Ran, J. Wang, Y. Ma, J. Mater. Sci. Technol. 168 (2024) 88–102, doi:10.1016/j.jmst.2023.02.064.

[14] M. Deng, L. Wang, D. Snihirova, J. Bohlen, G. Kurz, S.V. Lamaka, D. Höche, M.L. Zheludkevich, J. Magnes. Alloys 11 (2023) 1193–1205, doi:10.1016/j.jma.2022.12.014.

[15] W.R. Zhou, Y.F. Zheng, M.A. Leeflang, J. Zhou, Acta Biomater. 9 (2013) 8488–8498, doi:10.1016/j.actbio.2013.01.032.

[16] A. Srinivasan, C. Blawert, Y. Huang, C.L. Mendis, K.U. Kainer, N. Hort, J. Magnes. Alloys 2 (2014) 245–256, doi:10.1016/j.jma.2014.08.002.

[17] A. Srinivasan, Y. Huang, C.L. Mendis, C. Blawert, K.U. Kainer, N. Hort, Mater. Sci. Eng. A 595 (2014) 224–234, doi:10.1016/j.msea.2013.12.016.

[18] C. Dai, J. Wang, Y. Pan, K. Ma, Y. Peng, J. Ren, Y. Wang, D. Wang, J. Wang, Y. Ma, Corros. Sci. 210 (2023) 110806, doi:10.1016/j.corsci.2022.110806.

[19] C.Q. Li, D.K. Xu, Z.R. Zeng, B.J. Wang, L.Y. Sheng, X.B. Chen, E.H. Han, Mater. Des. 121 (2017) 430–441, doi:10.1016/j.matdes.2017.02.078.

[20] J. Xie, J. Zhang, Z. Zhang, Q. Yang, K. Guan, Y. He, R. Wang, H. Zhang, X. Qiu, R. Wu, Corros. Sci. 198 (2022) 110163, doi:10.1016/j.corsci.2022.110163.

[21] J. Dai, Q. Dong, Y. Nie, Y. Jia, C. Chu, X. Zhang, Mater. Des. 221 (2022) 110980, doi:10.1016/j.matdes.2022.110980.

[22] Y.M. Zhu, A.J. Morton, M. Weyland, J.F. Nie, Acta Mater. 58 (2010) 464–475, doi:10.1016/j.actamat.2009.09.025.

[23] Y.M. Zhu, A.J. Morton, J.F. Nie, Acta Mater. 58 (2010) 2936–2947, doi:10.1016/j.actamat.2010.01.022.

[24] J.F. Nie, Metall. Mater. Trans. A 43 (2012) 3891, doi:10.1007/s11661-012-1217-2.

[25] M. Yamasaki, Z. Shi, A. Atrens, A. Furukawa, Y. Kawamura, Corros. Sci. 200 (2022) 110237, doi:10.1016/j.corsci.2022.110237.

[26] Y. Nie, J. Dai, X. Li, X. Zhang, J. Magnes. Alloys 9 (2021) 1123–1146, doi:10.1016/j.jma.2020.09.021.

[27] C. Li, X. Li, X. Ke, Y. Dong, N. Wang, S. Wang, Z. Zhang, Corros. Sci. 228 (2024) 111829, doi:10.1016/j.corsci.2024.111829.

[28] J. Zhang, C. Xu, Y. Jing, S. Lv, S. Liu, D. Fang, J. Zhuang, M. Zhang, R. Wu, Sci. Rep. 5 (2015) 13933, doi:10.1038/srep13933.

[29] Y. Jiao, J. Zhang, P. Kong, Z. Zhang, Y. Jing, J. Zhuang, W. Wang, L. Zhang, C. Xu, R. Wu, M. Zhang, J. Mater. Chem. B 3 (2015) 7386–7400, doi:10.1039/c5tb01060h.

[30] J. Xie, J. Zhang, Z. Zhang, Z. Yu, Z. Xu, R. Wang, D. Fang, X. Zhang, X. Zhang, R. Wu, J. Mater. Sci. Technol. 151 (2023) 190–203, doi:10.1016/j.jmst.2023.01.005.

[31] Y. Zhang, Y. Huang, X. Chen, B. Luthringer-Feyerabend, J. Xue, D. Zander, R. Willumeit-Römer, K.U. Kainer, N. Hort, Scr. Mater. 212 (2022) 114509, doi:10.1016/j.scriptamat.2022.114509.

[32] Y. Wang, W. Xiao, C. Dai, J. Wang, F. Pan, Corros. Sci. 227 (2024) 111751, doi:10.1016/j.corsci.2023.111751.

[33] L. Yang, N. Hort, D. Laipple, D. Hoche, Y. Huang, K.U. Kainer, R. Willumeit-Römer, F. Feyerabend, Acta Biomater. 9 (2013) 8475–8487, doi:10.1016/j.actbio.2012.10.001.

[34] L. Yang, Y. Huang, Q. Peng, F. Feyerabend, K.U. Kainer, R. Willumeit-Römer, N. Hort, Mater. Sci. Eng. B 176 (2011) 1827–1834, doi:10.1016/j.mseb.2011.02.025.

[35] L. Yang, F. Feyerabend, K.U. Kainer, R. Willumeit-Römer, N. Hort, Mater. Sci. Forum 690 (2011) 417–421, doi:10.4028/www.scientific.net/MSF.690.417.

[36] L. Yang, Y. Huang, F. Feyerabend, R. Willumeit-Römer, K.U. Kainer, N. Hort, J. Mech. Behav. Biomed. Mater. 13 (2012) 36–44, doi:10.1016/j.jmbbm.2012.04.007.

[37] L. Yang, X. Zhou, S.-M. Liang, R. Schmid-Fetzer, Z. Fan, G. Scamans, J. Robson, G. Thompson, J. Alloys. Compd. 619 (2015) 396–400, doi:10.1016/j.jallcom.2014.09.040.

[38] L. Yang, L. Ma, Y. Huang, F. Feyerabend, C. Blawert, D. Hoche, R. Willumeit-Römer, E. Zhang, K.U. Kainer, N. Hort, Mater. Sci. Eng. C 75 (2017) 1351–1358, doi:10.1016/j.msec.2017.03.010.

[39] G. Bi, Y. Li, S. Zang, J. Zhang, Y. Ma, Y. Hao, J. Magnes. Alloys 2 (2014) 64–71, doi:10.1016/j.jma.2014.03.002.

[40] Q. Peng, J. Guo, H. Fu, X. Cai, Y. Wang, B. Liu, Z. Xu, Sci. Rep. 4 (2014) 3620, doi:10.1038/srep03620.

[41] F.R. Elsayed, N. Hort, M.A. Salgado-Ordorica, K.U. Kainer, Mater. Sci. Forum 690 (2011) 65–68, doi:10.4028/www.scientific.net/MSF.690.65.

[42] R. Hou, J. Victoria-Hernandez, P. Jiang, R. Willumeit-Römer, B. Luthringer-Feyerabend, S. Yi, D. Letzig, F. Feyerabend, Acta Biomater. 97 (2019) 608–622, doi:10.1016/j.actbio.2019.07.053.

[43] J. Bohlen, S. Meyer, B. Wiese, B.J.C. Luthringer-Feyerabend, R. Willumeit-Römer, D. Letzig, Materials (Basel) 13 (2020) 391, doi:10.3390/ma13020391.

[44] D. Baksh, R. Yao, R.S. Tuan, Stem Cells 25 (2007) 1384–1392, doi:10.1634/stemcells.2006-0709.

[45] S.V. Lamaka, B. Vaghefinazari, D. Mei, R.P. Petrauskas, D. Höche, M.L. Zheludkevich, Corros. Sci. 128 (2017) 224–240, doi:10.1016/j.corsci.2017.07.011.

[46] D. Hoche, C. Blawert, S.V. Lamaka, N. Scharnagl, C. Mendis, M.L. Zheludkevich, Phys. Chem. Chem. Phys. 18 (2016) 1279–1291, doi:10.1039/c5cp05577f.

[47] J.F. Nie, K. Oh-ishi, X. Gao, K. Hono, Acta Mater. 56 (2008) 6061–6076, doi:10.1016/j.actamat.2008.08.025.

[48] Z. Yu, X. Xu, B. Du, K. Shi, K. Liu, S. Li, X. Han, T. Xiao, W. Du, Acta Metall. Sin. Engl. Lett. 35 (2021) 596–608, doi:10.1007/s40195-021-01269-3.

[49] Y. Jang, B. Collins, J. Sankar, Y. Yun, Acta Biomater. 9 (2013) 8761–8770, doi:10.1016/j.actbio.2013.03.026.

[50] N.A. Agha, F. Feyerabend, B. Mihailova, S. Heidrich, U. Bismayer, R. Willumeit-Römer, Mater. Sci. Eng. C 58 (2016) 817–825, doi:10.1016/j.msec.2015.09.067.

[51] K. Munir, J. Lin, X. Tong, A. Biesiekierski, Y. Li, C. Wen, J. Magnes. Alloys 12 (2024) 546–572, doi:10.1016/j.jma.2024.02.002.

[52] X. Gu, Y. Zheng, Y. Cheng, S. Zhong, T. Xi, Biomaterials 30 (2009) 484–498, doi:10.1016/j.biomaterials.2008.10.021.

[53] J. Liu, D. Bian, Y. Zheng, X. Chu, Y. Lin, M. Wang, Z. Lin, M. Li, Y. Zhang, S. Guan, Acta Biomater. 102 (2020) 508–528, doi:10.1016/j.actbio.2019.11.013.

[54] E. Willbold, X. Gu, D. Albert, K. Kalla, K. Bobe, M. Brauneis, C. Janning, J. Nellesen, W. Czayka, W. Tillmann, Y. Zheng, F. Witte, Acta Biomater. 11 (2015) 554–562, doi:10.1016/j.actbio.2014.09.041.

[55] L. Li, Z. Zhang, D. Zhang, F. Qi, Y. Dai, W. Wei, X. Ouyang, J. Magnes. Alloys 13 (2025) 296–310, doi:10.1016/j.jma.2024.05.005.

[56] C.L. Liu, J. Jiang, M. Wang, Y.J. Wang, P.K. Chu, W.J. Huang, Adv. Mater. Res. 287 (2011) 2008–2014.

[57] R. Zhao, W. Zhu, J. Zhang, L. Zhang, J. Zhang, C. Xu, Mater. Sci. Eng. A 788 (2020) 139594, doi:10.1016/j.msea.2020.139594.

[58] G. Jiang, Y. Huang, S. Gavras, H. Shi, N. Hort, in: A. Leonard, S. Barela, N.R. Neelameggham, V.M. Miller, D. Tolnai (Eds.), BT-Magnesium Technology 2024, Springer Nature Switzerland, Cham, 2024, pp. 7–13.

[59] D. Mei, S.V. Lamaka, J. Gonzalez, F. Feyerabend, R. Willumeit-Römer, M.L. Zheludkevich, Corros. Sci. 147 (2019) 81–93, doi:10.1016/j.corsci.2018.11.011.

[60] D. Mei, S.V. Lamaka, C. Feiler, M.L. Zheludkevich, Corros. Sci. 153 (2019) 258–271, doi:10.1016/j.corsci.2019.03.039.

[61] S. Johnston, Z. Shi, A. Atrens, Corros. Sci. 101 (2015) 182–192, doi:10.1016/j.corsci.2015.09.018.

[62] R.-Q. Hou, N. Scharnagl, F. Feyerabend, R. Willumeit-Römer, Corros. Sci. 132 (2018) 35–45, doi:10.1016/j.corsci.2017.12.023.

[63] Q. Zhu, Y. Li, F. Cao, D. Qiu, Y. Yang, J. Wang, H. Zhang, T. Ying, W. Ding, X. Zeng, Nat. Commun. 13 (2022) 5838, doi:10.1038/s41467-022-33480-w.

[64] J. Speight, Lange's Handbook of Chemistry, Sixteenth Edition, The McGraw-Hill Companies, Inc, Wyoming, 2005.

[65] L. Yang, Y. Huang, F. Feyerabend, R. Willumeit-Römer, C. Mendis, K.U. Kainer, N. Hort, Acta Biomater. 9 (2013) 8499–8508, doi:10.1016/j.actbio.2013.03.017.

[66] D. Dvorský, J. Kubásek, K. Hosová, M. Čavojský, D. Vojtěch, Metals (Basel) 11 (2021) 728, doi:10.3390/met11050728.

[67] Y.M. Kim, C.D. Yim, H.S. Kim, B.S. You, Scr. Mater. 65 (2011) 958–961, doi:10.1016/j.scriptamat.2011.08.019.